



# Flexible fiber optoelectrodes integrating Perovskite-Nafion-ITO layers for efficient photoelectrocatalytic water purification

Tzu-Heng Wang<sup>a</sup>, Zhe Zhao<sup>c</sup>, Sergi Garcia-Segura<sup>c</sup>, Li Ling<sup>d</sup>, Ruey-an Doong<sup>b</sup>, Paul Westerhoff<sup>c,\*</sup>

<sup>a</sup> Department of Biomedical Engineering and Environmental Sciences, National Tsing Hua University, 101, Section 2, Kuang Fu Road, Hsinchu 30013, Taiwan, ROC

<sup>b</sup> Institute of Analytical and Environmental Sciences, National Tsing Hua University, 101, Section 2, Kuang Fu Road, Hsinchu 30013, Taiwan, ROC

<sup>c</sup> NSF Nanosystems Engineering Research Center for Nanotechnology-Enabled Water Treatment, School of Sustainable Engineering and the Built Environment, Ira A. Fulton Schools of Engineering, Arizona State University, Tempe, AZ 85287-3005, USA

<sup>d</sup> Advanced Interdisciplinary Institute of Environment and Ecology, Beijing Normal University, Zhuhai 519087, China

## ARTICLE INFO

### Keywords:

Indium tin oxide  
Perovskite  
Polymeric optical fiber  
Electrochemical advanced oxidation processes (EAOPs)  
Photoelectrocatalysis

## ABSTRACT

Photoelectrocatalytic processes (PECs) combine photocatalysis and electrochemical principles to enhance charge carrier generation and stability within nanomaterials (NMs). Nano-enabled PECs can be used for water purification or hydrogen production. While most PEC studies focus on nanomaterial discovery to improve charge carriers generation and separation, PEC reactor design is important to maximize energy efficiency of light delivery to activate photocatalysts. Current designs face challenges due to low energy efficiencies because most reactor designs orientate light sources perpendicular to flat photocatalyst-coated electrode surfaces, and light must pass through glass materials plus water. We developed a low-cost, physically flexible catalytic polymeric optical fiber (POF) architecture, called optoelectrode fibers, embedded with electrically-conductive indium tin oxide (ITO) nanomaterials (NMs) plus  $\text{TAB}_3\text{Bi}_2\text{Br}_7\text{I}_2$  perovskite (ABI) visible-photocatalysts in Nafion-PVDF polymers surface layer. The PEC-POF architecture achieves > 6000% larger surface area than flat glass electrodes, > 90% organic pollutant removal in water, and > 300% better incident photon-to-current than the same ABI-NM deposited on a conventional ITO-coated flat glass-plate under low energy irradiation. POFs are useful because are agonistic to the type of NM, facilitating deposition of NMs tunable to specific wavelengths using LED or polychromatic light sources. Bundling large numbers of POF optoelectrodes together achieves reactors with orders of magnitude higher packing geometries ( $\text{m}^2$  of catalyst surface per  $\text{m}^3$  of reactor volume) than flat-electrode PEC reactors, enabling the optoelectrode fiber to address environmental problems.

## 1. Introduction

Photoelectrocatalytic processes (PECs) are an emerging photo-assisted electrified technology for water purification or energy production that promote electrons of a semiconductor ( $e_{\text{CB}}^-$ ) from the valence band (VB) to the conduction band (CB) according to reaction (1). Given the different redox potentials with strong oxidizing holes ( $h_{\text{VB}}^+$ ) and reducing  $e_{\text{CB}}^-$ , PECs can be deployed either as advanced oxidation processes (AOPs) [1] or advanced reduction processes (ARPs) [2] to remediate the environmental pollutants by reactive oxygen species (ROS) (e.g., hydroxyl radical ( $\cdot\text{OH}$ ), and superoxide radical ( $\cdot\text{O}_2^-$ ) from reaction (2) and (3), or as a water-splitting reaction to yield  $\text{H}_2$  for renewable energy production [3].



Most PEC research has aimed to develop novel catalytic nanomaterials (NMs) with increased stability or energy conversion efficiency. Nevertheless, PEC reactor designs most commonly still rely upon flat electrodes (e.g., ITO or FTO plate) with light sources orientated perpendicular to the electrode surface, wherein artificial light or sunlight must pass through glass windows and then transmit through water before illuminating the NM coated electrode surface. The associated light attenuation reduces the amount of energy reaching the electrode

\* Corresponding author.

E-mail address: [p.westerhoff@asu.edu](mailto:p.westerhoff@asu.edu) (P. Westerhoff).

<https://doi.org/10.1016/j.apcatb.2023.123397>

Received 19 April 2023; Received in revised form 20 September 2023; Accepted 14 October 2023

Available online 16 October 2023

0926-3373/© 2023 Elsevier B.V. All rights reserved.

surface, especially in wastewaters with high light absorbance (i.e., low transmittance) [4,5]. Furthermore, a flat-plate photoelectrode also limits the total surface area that could be integrated into any larger scale reactor (i.e., geometric packing density characterized by units of  $\text{m}^2$  of catalyst surface per  $\text{m}^3$  of reaction volume) [6]. These two barriers of light management and harvesting dramatically limits PEC system efficiency, and is rapidly becoming a more urgent need than discovery of new catalytic materials. The aim of this paper is to demonstrate how a new optoelectrode design can achieve  $>10\times$  improvements in light harvesting and management through development of a high geometric packing density of light harvesting catalytic surfaces based upon recent advances in side-emitting optical fiber technology.

Optical fibers are among the most common light waveguides for flexible optoelectronic functional integration, such as photodetectors, lasers, and biosensors [7,8]. Light can be launched into optical fibers from concentrated sunlight, light-emitting diodes (LEDs), lasers, etc [9]. Because photons and evanescent wave energy from within the fiber strike its outer surface, placing NMs on the fiber surface eliminates light transmittance losses through water or glass reactor windows, and achieves higher quantum yields [8]. Additionally, the remarkable physical flexibility, ease to connect with a variety of light sources and photon transmission efficiency enable polymeric optical fibers (POFs) to be well suited in more complex designs and support photocatalysis by additional nanolayers in the solar spectrum [10,11].

Many emerging nanomaterials for PECs are visible-light activated, because longer wavelengths of light are available by solar sunlight or can be generated at low capital or energy costs using light emitting diodes (LEDs). Metal halide perovskites ( $\text{ABX}_3$  or  $\text{A}_3\text{B}_2\text{X}_9$ , where A, B, and X are cations, and halogen anions) are representative emerging photocatalysts with superior performance compared against conventional semiconductors such as  $\text{TiO}_2$ . Perovskites present superior charge carrier mobility, long diffusion lengths, high structural stability, and tunable absorption across a wide range of wavelengths in the visible light spectrum [12,13]. Moreover, perovskite stability under photon illumination and high conversion capability when reacting to other metal NMs show great potential to enhance PEC effects [14]. Hence, exploring novel perovskite-based PEC reactor architecture that improve light management is extremely attractive. Here we focus on combining perovskite and POFs to address growing challenges of organics destruction in polluted water supplies.

This research aimed to fabricate, characterize, and demonstrate how

low-cost POFs ( $<\$0.10$  USD per meter) with PMMA cores and PVDF cladding can readily be engineered into optoelectrodes using potential NMss, boosting light harvesting and achieving superior photo-electrical performance over conventional flat-based PEC reactor architectures. NMs are enmeshed within a specially created porous and conductive cladding on the POF surface that allows diffusion of water within the cladding. The PEC-POF optoelectrode design (Fig. 1a) contrasts with nearly all conventional photoelectrodes, wherein the latter requires light to pass through glass and water before irradiating electrode surfaces (Fig. 1b).

Using pre-synthesized NMs on our optoelectrodes allow enormous flexibility in catalyst choice and control of crystal lattice and other critical structures, while avoiding costly manufacturing steps (e.g., chemical or atmospheric deposition) [10] commonly employed in creating thin conductive films (e.g., ITO) on conventional electrodes. The optoelectrode fiber replaces traditional glass electrodes by improving light harvesting and delivery to the photocatalysis on the POF surface, through side-emission of light from within the fiber lumen. It reduces energy requirements and enhances reaction surface area. First, optoelectrode fabrication considered surface morphology of varying NMs (ITO and  $\text{TAB}_3\text{Bi}_2\text{Br}_7\text{I}_2$  perovskite) mass loadings on high surface area POF ( $14\text{ cm}^2$ ), which influenced light energy passing through the fiber, improving the side-emission and photon utilization. Second, each NM layer enhances PEC performance and IPCE effects of NM-Nafion-PVDF POFs were quantified. Third, nano-enabled POF optoelectrode degradation of a model organic pollutant (benzoate ion) demonstrated competitive EAOP application. Visible light catalyst  $\text{TAB}_3\text{Bi}_2\text{Br}_7\text{I}_2$  perovskite (ABI) was benchmarked against conventional photocatalyst ( $\text{TiO}_2$ ). Finally, photoelectrocatalytic NM modified-POF offer competitive material testing through innovative POF optoelectrodes.

## 2. Methodology

### 2.1. Chemical reagents

Tetrabutylammonium bromide ( $\geq 98\%$ ), tetrabutylammonium iodide ( $98\%$ ), bismuth bromide ( $\geq 98\%$ ), titanium dioxide ( $\text{TiO}_2$ ,  $99.5\%$ ), 4-chlorobenzoic acid ( $99\%$ ), acetone ( $99\%$ ), isopropanol ( $99\%$ ), sodium benzoate ( $99.95\%$ ), and sodium oxalate ( $\text{Na}_2\text{C}_2\text{O}_4$ ,  $\geq 99\%$ ) were supplied by Sigma-Aldrich. Sodium benzoate ( $99.95\%$ ), sodium oxalate

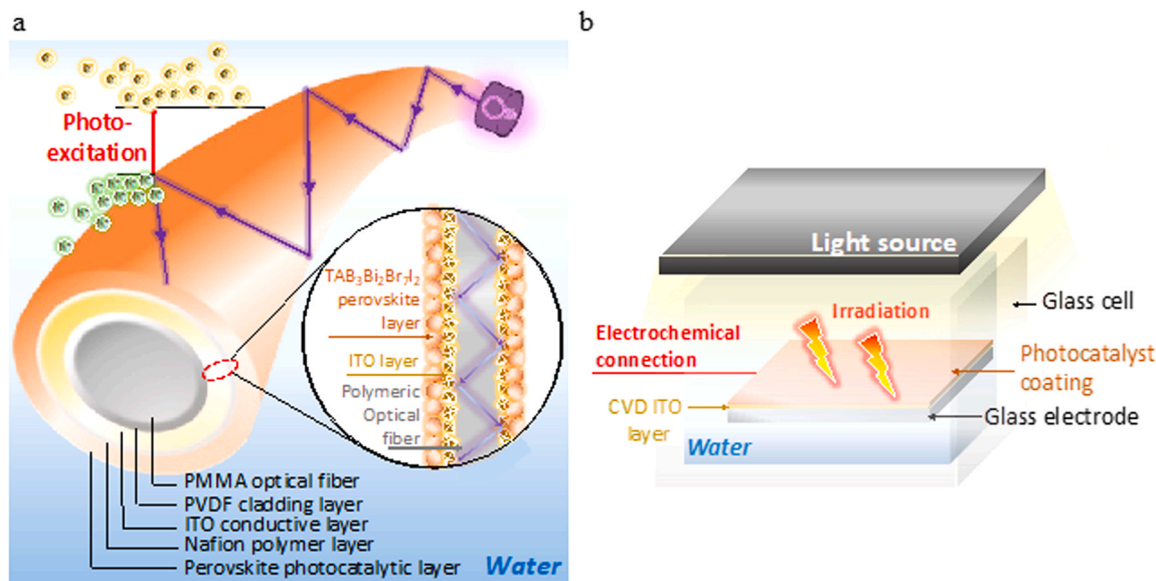


**Fig. 1.** Schematic illustration. (a) Novel reactor design with visible light delivered from a LED into a POF-ITO/ABI optoelectrode placed in a reactor containing water. (b) conventional reactor design where photons pass through a reactor cover and water before reacting photocatalysts deposited on ITO glass electrodes.

( $\geq 99\%$ ), Nafion (5% w/w in water and 1-propanol), *p*-benzoquinone (pBQ, 98%), and *tert*-butanol (tBuOH, 99%) were obtained from Thermo Fisher Scientific. All the other chemicals were of analytical grade and were used directly with any purification.

## 2.2. Preparing electrically conductive POFs by ITO nano-enabling

Side-emitting polymeric optical fibers (Model: 3925FT.50NA) were purchased from Fiber Optic Products (UT, USA). The POFs of 1.5 mm diameter consisted of a composite of two polymers: a poly (methyl methacrylate) core (PMMA) of 1470  $\mu\text{m}$  diameter with refractive index ( $n$ ) of 1.49, and a polyvinylidene difluoride (PVDF) outer layer of 30  $\mu\text{m}$  thick with  $n$  of 1.43. The difference in refractive indices between the two polymers results in side emission of light from the core of the fiber. POFs were cut into 30 cm lengths. Cut surfaces at both ends were polished using five optical polish films (LE30D, LE5P, LE3P, LE1P, LE03P, Thorlabs, Newton, NJ) until a specular surface was obtained. Polishing was conducted after cutting fibers and after modification of fibers with NMs. Fig. S1 show that the cut surfaces on both ends of bare and coated POFs had smooth surfaces required to decrease the interference when light is launched from the LED into the lumens, which is defined as the fiber's inner region where the light is transmitted through.

PMMA/PVDF polymers are not intrinsically electrically conductive. Therefore, the POFs were modified to implement conductive properties at their interfacial surface. Indium tin oxide (ITO) is a well-known semiconductor with optical transparency to visible light that is commonly used as conductive substrate for photoelectrodes. Indium tin oxide (ITO) nanoparticles (50 nm; 99.5% purity, US Research Nanomaterials Inc.) were used to coat POF following a similar method developed for other NMs. First, ITO powder was homogeneously dispersed in 15 mL of acetone and ultrasonicated within a Branson M5800 ultrasound bath for 30 min. Acetone induces plasticization by chain disentanglement of the PVDF polymer layer which enables ITO nanoparticle attachment by enmeshment on the POF surface. Second, the suspended solution quickly placed in a thin cylindrical container pipette shaped and the pristine POF submerged into the solution for 2 s and removed. Then, the acetone was quickly evaporated under atmospheric conditions. Finally, the ITO coated POFs were rinsed with ultrapure water and fully dried at 60  $^{\circ}\text{C}$  for 1 h. To achieve different mass loadings of ITO on the POF surface, different ITO suspended acetone solutions were prepared containing different mass loading of nanoparticles ranging from 0.5  $\text{g L}^{-1}$  up to 10.0  $\text{g L}^{-1}$ .

## 2.3. Deposition of nanomaterials to fabricate single-layer photocatalytic or dual-layer photoelectrocatalytic POFs

Optoelectrodes benefited from the use of  $\text{TAB}_3\text{Bi}_2\text{Br}_7\text{I}_2$  perovskite (ABI) or  $\text{TiO}_2$  photocatalysts. Details on the synthesis methods and characterization of pristine  $\text{TAB}_3\text{Bi}_2\text{Br}_7\text{I}_2$  perovskite nanomaterials are provided in supporting information (see Figs. S2-S4). Optoelectrodes were manufactured following a dip coating method using a photocatalyst suspension. The dispersion solution consisted of photocatalytic nanoparticles (i.e.,  $\text{TAB}_3\text{Bi}_2\text{Br}_7\text{I}_2$  perovskite or  $\text{TiO}_2$ ) in 15 mL of isopropanol containing 10 wt% of ionomer Nafion<sup>®</sup> that were sonicated for 1 h in ice bath before use to ensure homogeneous dispersion. Photoelectrocatalyst doses in the dispersion ranged from 3  $\text{g L}^{-1}$  up to 10  $\text{g L}^{-1}$ . The POF-ITO fibers were dip coated the selected solution for 2 s and air dried. Then, optoelectrodes were generously rinsed with ultrapure water and dried for 1 h at 60  $^{\circ}\text{C}$ . The final products consisted of POF-ITO/ABI or POF-ITO/ $\text{TiO}_2$  optoelectrodes. Similar procedures were followed to prepare blank fibers by using pristine POF instead of POF-ITO obtaining POF-ABI and POF- $\text{TiO}_2$  fibers.

For comparison to POFs, commercial ITO glass plate (3  $\times$  1  $\text{cm}^{-2}$ ; 100 nm ITO thick, Guluo China) were used as flat substrate for additional electrocatalyst characterization. The ITO glass electrodes were coated with ABIs and  $\text{TiO}_2$  following the same method described above

for POF coatings.

## 2.4. Material, optical and PEC characterization of fabricated optoelectrodes

The morphology and elemental composition of pristine and modified POF surfaces were assessed using a scanning electron microscope (JEOL JXA-8530 F) coupled with energy dispersive X-ray spectroscopy (EDS). The crystallographic planes and structures were evaluated by X-ray diffraction (XRD). The diffractograms were registered on a Malvern PANalytical Aeris X-ray Diffractometer for fibers with Cu K $\alpha$  radiation ( $\lambda = 1.5406 \text{ \AA}$ ) at a voltage of 40 kV and a current of 15 mA. The optical properties and band structure of ABIs are obtained on UV-Visible spectrophotometer (Hitachi U-4100) and ultraviolet photoelectron spectroscopy (UPS) to identify the adsorption wavelengths and valence band maximum (VBM).

The optical light transmittance and refraction optical properties for side emission of the POF and modified POF were evaluated through photon irradiance measurement. Optoelectrodes and pristine POFs were mounted on monochromatic UV-light LEDs ( $\lambda = 395 \text{ nm}$ ) of 2.18 W set at 3.48 V and irradiance of 29  $\mu\text{W cm}^{-2}$ . Light output in terms of irradiance ( $\mu\text{W cm}^{-2}$ ) was measured by a spectrophotometer (Avantes AvaSpec-2048 L (Louisville, CO) [9].

Electrochemical (EC) and photoelectrochemical (PEC) characterizations were conducted using a potentiostat (Autolab PGSTAT302N from Metrohm (USA)) operated with Nova 2.1.1 software. Electroanalytical characterizations were carried out in a three-electrode system consisting of a platinum wire as counter electrode, Ag/AgCl as the reference electrode, and different working electrodes of 1  $\text{cm}^2$  geometric area: POF-ITO, POF-ITO/ABI and POF-ITO/ $\text{TiO}_2$ . Ultrapure water solutions containing 1.0 M  $\text{Na}_2\text{SO}_4$  as supporting electrolyte at pH 6.8 de-aerated with nitrogen gas were used in all the (photo)electrochemical characterization measurements. Irradiation source used in photo-assisted experiments consisted of the same UV-light LEDs ( $\lambda = 395 \text{ nm}$ ) of 2.18 W with a spectral width of 40 nm in 120 radiation angles. Cyclic voltammetric (CV) and linear sweep voltammetry (LSV) analyses were recorded in the potential range of 0.0–1.2 V vs Ag/AgCl with scan rate of 5  $\text{mV s}^{-1}$  in the dark or under light irradiation. Photocurrent density stability was studied by operating chronoamperometry (CA) measurements at an applied potential of 1.2 V vs Ag/AgCl with on/off irradiation cycles of 60 s each.

Incident photon-to-current efficiency (IPCE) measurements evaluate the ratio of the photocurrent vs. the rate of incident photons as a function of wavelength. The IPCE values were estimated under a constant potential bias of 1.2 V vs. RHE following Eq. (4):

$$IPCE(\%) = \frac{J_{ph} \times 1239.8}{I_{input} \times \lambda} \times 100 \quad (4)$$

where  $J_{ph}$  ( $\text{mA cm}^{-2}$ ) is the obtained photocurrent density at the specific incident-light wavelength ( $\lambda$ , nm), 12,398 ( $\text{V} \times \text{nm}$ ) is the constant via  $h$  (Planck's constant) multiplied by  $c$  (speed of light),  $I_{input}$  is the irradiance of the monochromatic LED [2].

## 2.5. PEC experiments using an organic pollutant in water

The competitiveness of the optoelectrodes to be applied in electrochemical advanced oxidation processes (EAOPs) was assessed through the photoelectrocatalytic degradation of benzoate ion. Experiments were conducted in a batch reactor consisting of a cylindrical electrochemical cell containing 50 mL of 261  $\mu\text{M}$  sodium benzoate solution and 0.5 M  $\text{Na}_2\text{SO}_4$  electrolyte at pH 6.8. Solutions were kept under vigorous stirring at 350 rpm to ensure transport from/towards the optoelectrode during treatment. The optoelectrodes were operated with a monochromatic UV-light LEDs ( $\lambda = 395 \text{ nm}$ ) of 2.18 W set at 3.48 V and irradiance of 29  $\mu\text{W cm}^{-2}$ . The same set-up was used to conduct blank



experiments of photocatalysis (without application of a bias potential) and electrocatalysis (without UV-light irradiation). Aliquots of solution were collected over time and benzoate ion quantified by chromatographic analyses of a high-performance liquid chromatograph (HPLC) (Waters 2695) coupled to a photodiode array detector (Waters 2998) set at 225 nm. The HPLC was fitted with a Waters LiChrosorb 10  $\mu\text{m}$  column (Diameter: 4.0 mm; Length: 25 cm). Separation was conducted using a mobile phase consisting of water:acetonitrile (70:30) at 25  $^{\circ}\text{C}$  with a flow rate of 1.0  $\text{mL min}^{-1}$ . The injection volume was 10  $\mu\text{L}$ . Chromatograms illustrated well-defined peaks of benzoate at retention times of 2.1 min. Degradation kinetics in benzoate ion over time showed excellent fittings for pseudo-first order rate kinetics. The percentage of benzoate degradation was quantified from Eq. (5):

$$\text{Removal}(\%) = \frac{C_t - C_{t=0}}{C_{t=0}} \times 100 \quad (5)$$

ROS experiments were performed in the presence of appropriate radical scavenging compounds, including sodium oxalate ( $\text{Na}_2\text{C}_2\text{O}_4$ ) for holes, *p*-benzoquinone (pBQ) for superoxide radicals, and *tert*-butanol (tBuOH) for hydroxyl radicals, to determine the reactive species and electrons/holes' redox reaction in the PEC degradation of benzoate ion addition [15,16].

### 3. Results and discussions

#### 3.1. Characterization of the morphology and elemental distribution of indium tin oxide (ITO) and $\text{TAB}_3\text{Bi}_2\text{Br}_7\text{I}_2$ perovskite layers

Electron microscope images were obtained for the exterior surface and elemental mapping of uncoated POF, POF-ITO and POF-ITO/ABI. The surface of the uncoated bare POF only contains carbon, oxygen and fluorine, which comprise the PVDF POF cladding (Fig. 2a). After the dip-coating of ITO, the POF-ITO exhibited a uniform thin deposited layer containing indium and tin distributed on the fiber surface (Fig. 2b). The POF-ITO/ABI optoelectrode exhibited a homogenous coverage with bismuth, bromine, and iodine in Fig. 2c. Fig. S1 demonstrated that after cleaving the POF-ITO/ABI optoelectrode, and confirmed successful deposition of NMs evenly distributed along the outside surface of POFs.

XRD diffractograms of POF-ITO, as shown in Fig. S5a for different mass loadings, confirm the presence of characteristic peaks of ITO thin film on the optical fibers at  $21.7^{\circ}$ ,  $30.8^{\circ}$ ,  $35.7^{\circ}$ , and  $51.9^{\circ}$   $2\theta$  that are associated to the (211), (222), (400), and (440) planes of crystalline ITO [10,17]. Thus, the ITO dip-coating fabrication retains original crystallinity without any peak shifting. Likewise, after decorating ABI onto the POF-ITO (Fig. S5b), the XRD pattern exhibits additional peaks at  $25.2^{\circ}$

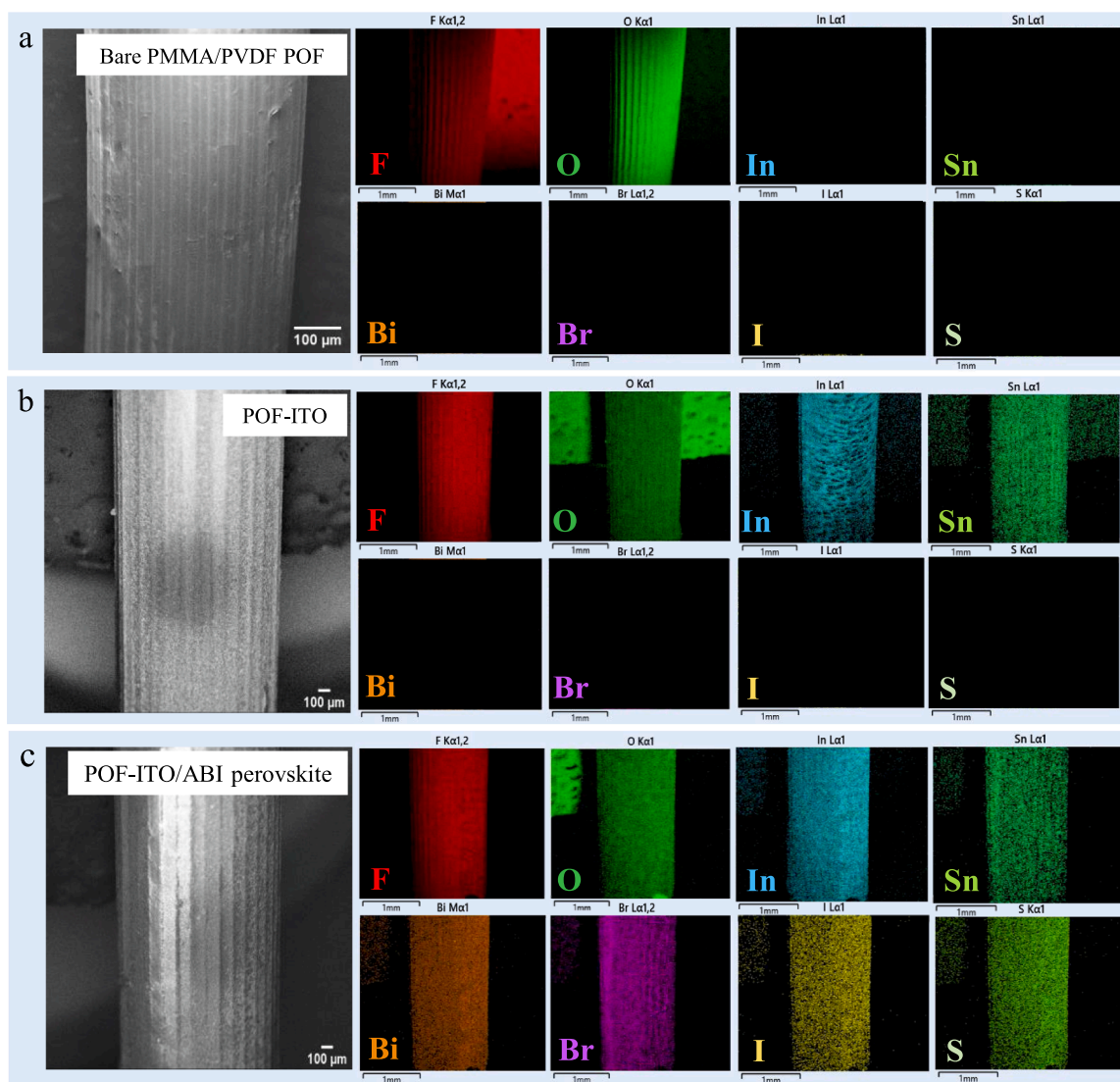


**Fig. 2.** Characterization and analysis of uncoated polymeric optical fibers, POF-ITO, and POF-ITO/ABI. Scanning electron microscope (SEM) surface images and energy dispersive X-ray spectroscopy (EDS) element distribution of (a) uncoated polymeric optical fibers; (b) POF-ITO; (c) POF-ITO/ABI.

and  $51.7^\circ 2\theta$  belonging to the (006) and (0012) crystal plane, which are corresponding to the *c*-directional growth of perovskite structure [18]. Moreover, a strong peak signal of ABI was detected at  $32.1^\circ$  suggesting the presence of (210) plane of cubic perovskite in  $A_3B_2X_9$  formation, which results from the fixed atomic positions of indium in the tetragonal phase [19]. SEM/EDS and XRD analyses confirm the successful fabrication of modified cladding/surface on the bare POF via dip-coating without changes in NM crystalline structures, demonstrating exceptional stability on the POF.

### 3.2. Effects of nanomaterial mass loadings on POFs on side-emitted visible light and light utilization efficiency

POFs side-emit light at 395 nm due to differences between refractive indices (*n*) of the PMMA core ( $n = 1.49$ ) and 30  $\mu\text{m}$  thick PVDF coating ( $n = 1.43$ ). As a result of the smooth and evenly textured outer surface, the bare POF has a low intensity of side-emitted light along the 30 cm length (i.e.,  $1230 \mu\text{W cm}^{-2}$  maximum at the proximal end and  $36 \mu\text{W cm}^{-2}$  at the terminal end) (Fig. S6a); this provided a baseline value for side-emitted energy light.

Side-emission of light was enhanced by integrating of NMs into the PVDF layer. Compared to the bare POF, the addition of a thin ITO layer (mass loading of  $8 \mu\text{g ITO cm}^{-1}$  fiber) on the POF resulted in a slight enhancement of side emission from  $1230$  to  $1620 \mu\text{W cm}^{-2}$ . This was attributed to (i) changes of refractive index of the coating; (ii) ITO serving as additional scattering centers; and (iii) evanescent wave interacting between ITO NMs and fiber interface [9]. Fig. S6a demonstrates the impact of increasing ITO loading on the amount of light side-emitted along the length of the fiber. The highest ITO loading ( $73 \mu\text{g cm}^{-1}$ ) resulted in the most significant side emission, approximately 7x higher than the side emission of the bare fiber. The side emission decreased exponentially from a maximum of  $8120 \mu\text{W cm}^{-2}$  at the proximal end of the modified POF to  $230 \mu\text{W cm}^{-2}$  at the terminal end).

The side-emitted light allows the NMs within the PVDF coating of the POF to be excited, leading to photon-driven reactions. The measurement of side-emitted light in our study represents the "excess" light that is not efficiently harvested but instead serves as an indicator of increased photon delivery to NMs within the PVDF/Nafion interlayer. This increased photon delivery allows for more efficient absorption and utilization of the light as it passes through the catalyst layers. Overall, incorporating ITO materials into or onto the PVDF surface increased the side-emission performance. This improvement is attributed to the excellent transparent property (i.e.,  $\geq 85\%$ ) and its ability to extend light absorption (i.e., UV-to-visible light spectrum) of ITO NMs. Such advancements pave the way for future experiments exploring dual-layer NM coating, where the enhanced side-emission can potentially boost the excitation of photocatalysts deposited atop the ITO layer.

For comparison, coating ABI on POF resulted in greater enhancements of side-emitted light than an ITO coating, which displayed 1.4x higher in the similar mass loading of NMs. For example, Fig. S6b shows that POF-ABI with a  $60 \mu\text{g cm}^{-1}$  loading (i.e.,  $5 \text{ g ABI L}^{-1}$ ) exhibited higher side-emitted light profiles than POF-ITO i.e., mass loading of  $61 \mu\text{g cm}^{-1}$ . These side emission results suggest that the size or composition of NMs, which influences refractive indexes and overall light scattering behaviors, is a more important factor than particle mass loading in the PVDF layer.

However, efficient optoelectrode operation requires more than just high levels of side-emitted light. The choice of materials is also crucial to enable interfacial layer conductance (i.e., ITO) and visible light photo-activity (i.e., ABI). Therefore, to create a fiber with both photo-active and conductive properties, two types of NMs were incorporated into the surface of the POF. Fig. S6c shows side-emission measurements for POFs modified by ITO or ITO plus ABI. Increasing mass loadings of ABI ( $10 \mu\text{g cm}^{-1}$ ) on POF-ITO ( $65 \mu\text{g cm}^{-1}$ ) lead to a 6x enhanced side-emission at the proximal end from  $1830 \mu\text{W cm}^{-2}$  to  $11,700 \mu\text{W cm}^{-2}$ .

Based on a comparison between the two modified optical fibers, the deposition of the second layer of photocatalysts successfully improved the side-emitted light through the dual-layer of NMs.

An energy balance on light throughout the fiber provides unique insights into efficiency of POFs. The overall light input entering the optical fiber ( $I_0$ ) is distributed according to Eq. (6), where  $I_0$  ( $\mu\text{W cm}^{-2}$ ) was measured with bare POF using a 2-cm length fiber.  $I_T$  ( $\mu\text{W cm}^{-2}$ ) measured the irradiance on the bottom surface of the fiber, which is transmitted through the fiber to the tip (i.e., the light escaping from the bottom of the fiber). The value of  $I_{\text{Abs}}$  (%) signified the portion of entering light absorbed by the polymer layers (i.e., PMMA + PVDF layer) and was calculated using Eq. (7), with  $I_0$  subtracting to  $I_S$ ,  $I_T$ , and  $I_U$  (i.e.,  $I_U$  equals zero (%) in bare POF since no NMs deposited on the bare POF) in uncoated POF. To quantitatively compare the total amount of side emitted light along the length of the fiber relative to light entering the fiber, the  $I_S$  and  $I_U$  (%) were calculated by following Eqs. (8) and (9), respectively (Table S1).

$$I_0 = I_S + I_U + I_T + I_{\text{Abs}} \quad (6)$$

$$I_{\text{Abs}}(\%) = \frac{I_0 - I_T - I_S - I_U}{I_0} \times 100\% \quad (7)$$

$$I_S(\%) = \frac{\int_0^L I_S dL}{I_0} \times 100\% \quad (8)$$

$$I_U = \frac{I_0 - I_S - I_T - I_{\text{Abs}}}{I_0} \times 100\% \quad (9)$$

where  $I_S$  is the irradiance scattered by the various refractive indices in the multiple NM layers, calculated as the integrated 3-dimensional irradiation "cone" of the energy side emitted along an equivalent length (30 cm) of the cylindrical-shaped POF, where  $I_0$  ( $\mu\text{W cm}^{-2}$ ) is the light energy entering the fiber. Last,  $I_U$ (%), the irradiance absorbed/ utilized by the photoelectrocatalytic layer, calculated by  $I_0$  subtracting the other three parameters.

A higher  $I_S$  is desirable, because it assures photo-activation of NMs throughout the POF surface layer. Fig. 3a shows  $I_S$  increased to 13% when prepared with higher NMs mass loading of ITO (i.e.,  $73 \mu\text{g cm}^{-1}$ ). Comparable  $I_S$  efficiencies were observed for single NM coating (i.e., ITO alone or ABI alone), the POF-ABI ( $67 \mu\text{g cm}^{-1}$ ) displays a significantly increasing in  $I_S$ , which is 2.1x higher than POF-ITO ( $73 \mu\text{g cm}^{-1}$ ). However, a 20% decrease in  $I_S$  is observed when the mass loading of ABI increased to  $70 \mu\text{g cm}^{-1}$ ; this is most likely due to an excessive amount of NMs and/or aggregation of NMs within the POF surface layer, causing obstruction or scattering of light back into the lumen.

The mass loading of ABI was then adjusted to maximize the side-emitted light of the POF-ITO/ABI, which would increase photo-excitation of the NMs on the POF surface. Fig. 3b shows a gradual increase in  $I_S$  (44%) from for POF-ITO/ABI up to  $17 \mu\text{g cm}^{-1}$  mass loading of perovskite, followed by a slight decrease in  $I_S$  (39%) for the higher mass loading of ABI ( $30 \mu\text{g cm}^{-1}$ ). Notably, the highest  $I_S$  occurred when two layers of NMs (ITO plus ABI) were coated onto the POFs. Using these optimized coatings ( $68 \mu\text{g cm}^{-1}$  ITO +  $25 \mu\text{g cm}^{-1}$  ABI with Nafion), we proceeded to investigate the number of coating cycles required to achieve homogeneous deposition of photocatalytic layers on POF-ITO. Figs. S6d and S7a demonstrated the highest  $I_S$  (58%) were achieved with 3 coating cycles using the optimized solution ( $75 \mu\text{g cm}^{-1}$  ITO +  $25 \mu\text{g cm}^{-1}$  ABI). Based on the superior performance in terms of  $I_S$ , this modified POF was selected for further experiments, and in subsequent calculation of the light utilization efficiency ( $I_U$ ) based upon Eq. (6).

Fig. S8 illustrates that the  $I_U$  increased to 11% and 16% when the deposition of ITO NMs ( $73 \mu\text{g cm}^{-1}$ ) and ABI ( $67 \mu\text{g cm}^{-1}$ ) on the POF. In Fig. 3b, the highest  $I_U$  (37%) was achieved using a dual-NM coating with the first ITO layer ( $75 \mu\text{g cm}^{-1}$ ) followed by an ABI layer ( $25 \mu\text{g cm}^{-1}$ ) in three layers. Both ITO NMs and ABI efficiently "utilize" light in the PVDF layer through absorption, reaction, and/or scattering,

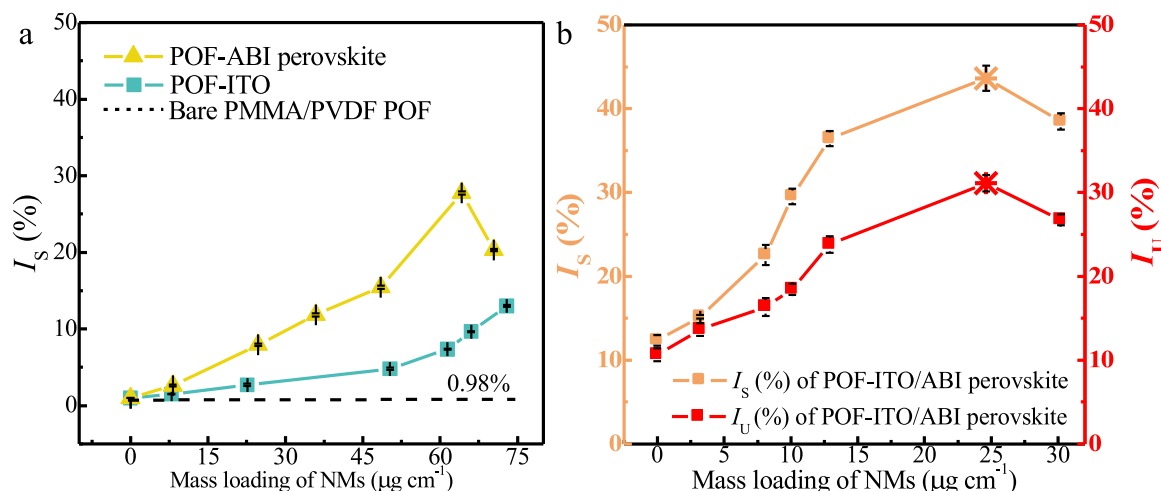


**Fig. 3.** Optical measurements of bare PMMA/PVDF POF, POF-ITO, POF-ABI, and POF-ITO/ABI. (a)  $I_s$  performance of modified POFs in different mass loading for single NM coating; (b)  $I_s$  and  $I_U$  effects of ABI atop ITO NM layer ( $68 \mu\text{g cm}^{-1}$ ) with 395 nm LED light (2.18 W) irradiation.

leading to the significant improvement in  $I_s$  and  $I_U$ . The dual NM layer (ITO + ABI) greatly increased side-emitted light on the fiber surface, enhancing the absorption/utilization capability ( $I_U$ ) between the photocatalyst layers and incident/scattered light. This modified POF with the dual-NM layer (ITO + ABI) was considered the "optimized" POF for PEC experiments.

### 3.3. Synergistic effects of ITO and ABI coatings on POFs for enhanced conductivity and photo-electrocatalytic activity

To establish that ex-situ synthesized ITO NMs coated into the PVDF layer of the POF can create a photo-anode, we quantified the impact of ITO coatings on the ability of polymer fibers to conduct electricity (i.e., applied potential at 0.0 – 1.2 V vs. Ag/AgCl) in the absence of light within our reactor containing a 0.5 M  $\text{Na}_2\text{SO}_4$  electrolyte solution. Fig. 4a shows LSV current density measurements for a bare POF and six different POF-ITO, fabricated through multiple coating cycles using a 10 g ITO  $\text{L}^{-1}$  acetone solution. As expected, there was no measurable current density for the bare POF, which is comprised of non-conductive PMMA fiber core and PVDF coating. POF-ITO with 3 or 4 coating cycles achieved the highest current density ( $0.18 \text{ mA cm}^{-2}$ ) with 71 and  $74 \mu\text{g cm}^{-1}$  ITO mass loading, respectively. However, increasing the ITO

loading through additional acetone-based NM solution coating cycles did not increase current density (Fig. 4a). Excessive coating cycles caused near complete dissolution of the PVDF layer, leading to loss of conductivity as shown in Table S1. The ITO loading in POF-ITO decreased to  $14 \mu\text{g cm}^{-1}$  after 5 cycles and completely disappeared in the sixth cycle of coating. These experiments confirmed the capability of ITO NMs to create electro-conductive POFs via multiple optimized coating cycles. Furthermore, in order to illustrate the current response stability of the optimal conductive optoelectrode, we assessed the robustness of the POF-ITO ( $73 \mu\text{g cm}^{-1}$ ) through ten successive electrochemical experiments with an applied potential of 1.2 V vs. Ag/AgCl. As depicted in Fig. S9, the electrical-conductivity performance remained relatively stable throughout the ten repeated cycles, with a consistent current density range of  $0.18 - 0.17 \text{ mA cm}^{-2}$ . Therefore, the optoelectrode appears stable from a material performance viewpoint, and future work will explore stability over thousands of operational cycles.

Photo-conductivity of POF-ITO/ABI quantified using CV and LSV analysis with different mass loadings of ABI perovskite on the POF-ITO surface. Perovskites provide several optical/electronic advantages (e.g., high catalytic activity, tunable redox property, and light absorption ability), which can increase electrical conductivity and photocurrent response under electrocatalysis and photoelectrocatalysis, respectively.

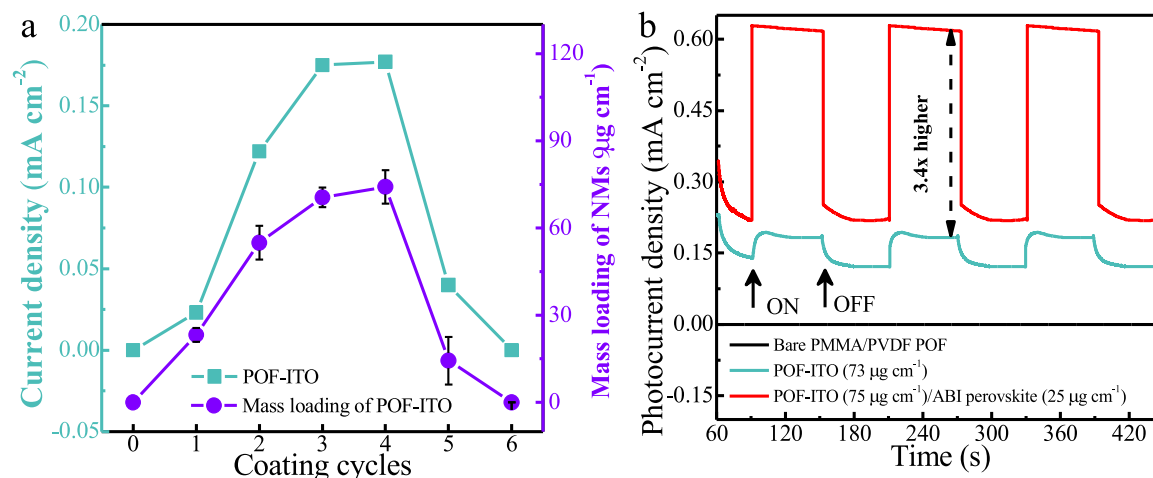


**Fig. 4.** Electrochemical and photo-electric performance in the pristine POF and integrated optoelectrode fibers. (a) conductive performance by LSV analysis of bare POF (0 coating layers) and six different POF-ITO produced using multiple coating cycles of  $10 \text{ mg ITO mL}^{-1}$  in 0.5 M  $\text{Na}_2\text{SO}_4$  electrolyte solution at pH 6.8; (b) photoelectrocatalytic stability of bare fiber, POF-ITO, and POF-ITO/ABI in 3 layers coating were recorded in chronoamperometry (CA) with 395 nm LED light (2.18 W) irradiation.



The highest current density of  $0.66 \text{ mA cm}^{-2}$  was achieved for POF-ITO ( $75 \mu\text{g cm}^{-1}$ )/ABI ( $25 \mu\text{g cm}^{-1}$ ), which was 10% higher than the ABI-ITO glass plate in the conventional optoelectrode configuration (Fig. S11a).

Fig. 4b shows that the modified optoelectrode has an enhanced photocurrent density for the dual-NM coated POFs by the CA experiment at an applied potential of 1.2 V vs. Ag/AgCl. Additionally, the current response recorded under dark conditions corresponds to the pure electrochemical response of the polarized optoelectrode with the same bias potential above. The photocurrent density was 3.5 times higher for the mass loadings of  $75 \mu\text{g cm}^{-1}$  ITO plus  $25 \mu\text{g cm}^{-1}$  ABI compared with ITO only. This improvement plays a pivotal role in advancing the integration of light-driven photocatalysts within our integrated optoelectrode fiber system. This integration facilitates excitation through visible light irradiation, leading to the production of photo-excited electrons. Subsequently, these electrons are propelled by a positive electric field from the POF-ITO/ABI anode towards the cathode, significantly enhancing the conductivity response. The stable photocurrent observed over multiple cycles with the LED on, and minimal response without light (LED off), can be attributed to the integrated optoelectrode facilitating electron migration on the surface of POF-ITO/ABI. To further explore the stability and current response of the POF electrode, we carried out photo/current measurements on both the pristine POF and the POF subjected to 1000 cycles of flexible electrode bending at an angle of  $120^\circ$ . Fig. S12 presents the results, revealing that the current density performance remained consistently high, approaching 100%, for both optoelectrode fibers. This demonstrates the exceptional structural durability of the POF electrodes, even after enduring repeated physical bending. The PEC analysis highlights the synergistic and tunable nature of using both ITO and ABI NMs on the surface of POFs to improve charge transfer efficiency. However, it should be noted that ABI is not the only candidate that can function as a PEC.

The POF-ITO platform's robustness was demonstrated by comparing the photocatalytic response of ABI against commercial  $\text{TiO}_2$ , a widely studied photocatalyst [7,19,20]. Fig. S11a shows the POT-ITO/ $\text{TiO}_2$  ( $75 \mu\text{g ITO cm}^{-1}$  plus  $21 \mu\text{g TiO}_2 \text{ cm}^{-1}$ ) achieved a photocurrent density of  $0.55 \text{ mA cm}^{-2}$ . This response is slightly lower response than for the POF-ITO/ABI optoelectrode with similar NM loadings ( $75 \mu\text{g ABI cm}^{-1}$  plus  $25 \mu\text{g ITO cm}^{-1}$ ). This result demonstrates the flexible nature of POFs to embed various types of photocatalysts. Therefore, selecting the appropriate catalyst will be crucial in maximizing the photoelectrocatalytic response driven by visible-light irradiation.

### 3.4. Quantifying photoconversion with incident photon-to-current efficiency (IPCE) analysis of POF-ITO/ABI

To evaluate the photo-response properties of PEC performance across a wide range of incident monochromatic light, the Incident Photon-to-Current Efficiency (IPCE) value can provide insights into the performance of the PEC system from UV to VIS wavelengths [21,22]. Fig. 5 shows the IPCE results for the bare POF, POF-ITO, and POF-ITO/ABI coatings under various incident monochromatic lights. The bare POF demonstrated negligible IPCE, indicating its inability to conduct a current (i.e., applied potential at 1.2 V vs. Ag/AgCl). At a wavelength of 340–410 nm, the incident photon-to-current efficiency (IPCE) of the POF-ITO ( $73 \mu\text{g cm}^{-1}$ ) coating only increased slightly by 6%. However, when ABI ( $25 \mu\text{g cm}^{-1}$ ) was added to the POF-ITO coating, the IPCE efficiency significantly increased to 21%, which is 3.2x higher than that of the POF-ITO coating. The data also shows that for the POF-ITO/ABI optoelectrode, the IPCE responding wavelengths were extended up to 550 nm. This improvement can be attributed to ABI's exceptional visible-light response, which enhances the conversion rates between photons and current.

To demonstrate the superiority of the modified optoelectrode design compared to a conventional glass plate PEC design, both were loaded equal ABI mass loadings ( $\sim 23 \mu\text{g cm}^{-1}$ ) and IPCE measurements were

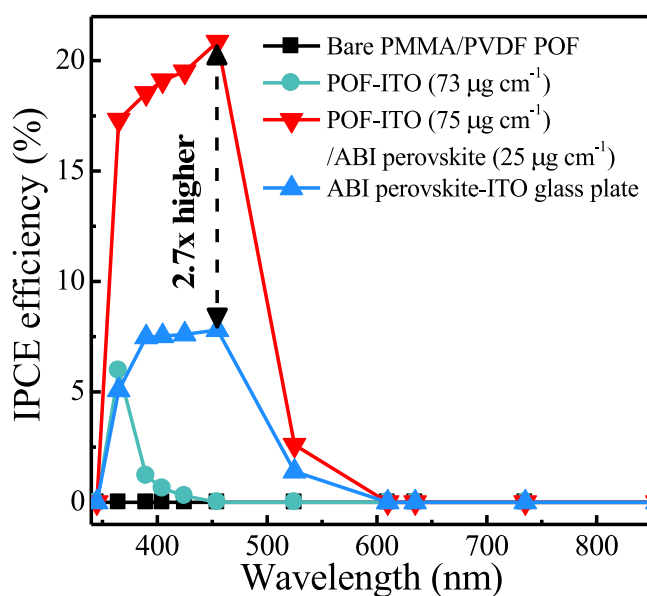


Fig. 5. Conversion efficiency of uncoated POF and modified POF plus NMs. Incident photon to current efficiency (IPCE) performance of bare PMMA/PVDF POF, POF-ITO, POF-ITO/ABI, and ABI ( $9 \text{ g L}^{-1}$ )-ITO glass plate.

performed. As demonstrated in Fig. 5, the POF-ITO/ABI optoelectrode exhibited nearly 300% higher efficiency than the ABI-ITO glass plate due to the superior reactive capability of the nanoparticles (NMs) deposited on the fiber surface. These results highlight the potential of our dual-coated POFs as optoelectrodes across a wide spectrum, with high light-harvesting capability that enhances the interaction between photons and current.

### 3.5. Pollutant degradation in water using optimized ITO plus ABI as a PEC-POF

Photoelectrochemical POF optoelectrodes possess the capability to drastically enhance  $\text{e}^- \text{h}^+$  pairs separation and effectively prevent recombination. Even though the relevance of the superoxide radical pathway decreases due to charge carrier separation by the electrical field, it further dramatically enhances the formation of the stronger oxidant, the hydroxyl radical, for transforming organic pollutants in water. POF optoelectrodes generate ROS to transform organic pollutants in water. Benzoate ion served as a model for other pollutants due to its well-established oxidation mechanism via ROS. The PEC-POF platform ( $75 \mu\text{g ITO cm}^{-1}$  +  $25 \mu\text{g ABI cm}^{-1}$ ) achieved 92% benzoate degradation in 60 min, with a pseudo first-order degradation rate constant ( $k$ ) of  $9.7 \times 10^{-4} \text{ s}^{-1}$ . POF-ITO with ABI demonstrated a 250% higher  $k$  value than ITO alone, indicating more efficient light energy and ROS utilization. Additionally, POF-ITO with ABI showed a 1.4x higher  $k$  value than when coated with  $\text{TiO}_2$  ( $21 \mu\text{g cm}^{-1}$ ), highlighting the superior photocatalytic ability of ABI over  $\text{TiO}_2$  due to its broader absorption wavelength from UV to visible light, making it easily photoactivated by the 395 nm LED.

To confirm that ROS ( $\text{h}^+$ ,  $\cdot\text{O}_2$ , and  $\cdot\text{OH}$ ) are the primary agents responsible for the degradation of benzoate ion, common radical quenching agents ( $\text{Na}_2\text{C}_2\text{O}_4$ , pBQ, and tBuOH) were added during the experiments [15,16]. Fig. 6a shows that the addition of  $0.01 \text{ mol L}^{-1}$   $\text{Na}_2\text{C}_2\text{O}_4$ , pBQ, and tBuOH resulted in a decrease of 35%, 80%, and 52% benzoate ion concentrations after 60 min, respectively. The  $k$  was observed to decrease by a factor of 1.3x to 4.5x in the presence of a scavenger, compared to experiments conducted without a scavenger ( $k = 9.7 \times 10^{-4} \text{ s}^{-1}$ ) (Figs. S13). ROS scavenger findings indicated that  $\text{h}^+$  and  $\cdot\text{OH}$  are the main ROS to react with benzoate ion in the PEC reaction, simultaneously  $\cdot\text{O}_2$  as assistance to accelerate the destructed

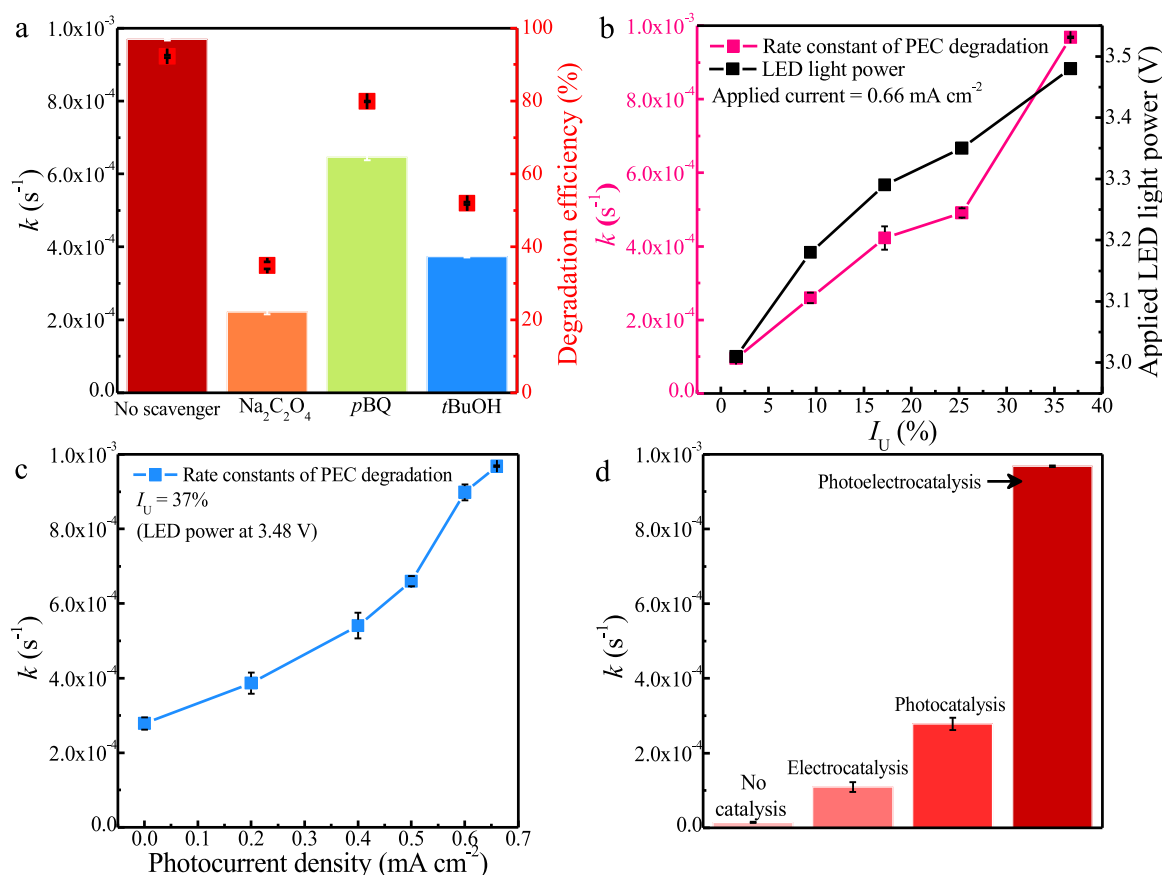


**Fig. 6.** Pseudo-first order comparison of benzoate ion. (a) effect of different scavengers for benzoate ion in the POF-ITO/ABI under photoelectrocatalysis of  $k$  and degradation efficiency after 60; Comparing the rate constants within (b) varying the LED light power (different  $I_U$  (%)); (c) adjusting the current density; (d) applying the different catalytic processes.

process. This finding is consistent with previous research on photoelectrocatalysis [23,24]. However, it is important to note that these results are significant for demonstrating the precise mechanisms that occur within the porous polymer-NM coating of our novel PEC-POF system.

The NM-Nafion-PVDF coating allows solutes and/or ROS to permeate the active NM polymer layer. Negligible benzoate ion adsorption occurred in control experiments, suggesting diffusion into the POF coating and reactions or ROS diffusion to degrade the pollutant. Previous research demonstrated porogen-modified PVDF with  $TiO_2$  effectively degrading other model pollutants. [25]. For additional information, please refer to Table S3 which summarizes the range of organic pollutants that can be degraded through photocatalyst modification using quartz and polymeric optical fibers. Previous PEC systems have only utilized glass optical fibers, whereas we have demonstrated polymeric optical fibers, which are more affordable and simpler to manufacture in PEC systems. This approach not only extends the light-harvesting range to the visible light spectrum but also simplifies the construction of conductive fibers. Other studies have used polymer fibers, but only in a PC mode. Our research (as shown in Fig. 6) demonstrates the potential for significantly increased pollutant degradation in PEC mode, as compared to PC mode.

In our study, we aimed to investigate not only the impact of NM type and loadings within the NM-modified POFs but also the role of light irradiance, applied currents, and fiber reusability. The PEC experiment controlled the same applied potential of 1.2 V vs. Ag/AgCl in electrocatalysis, and variable light intensities were produced by adjusting the power level (3.01–3.48 V) of the 395 nm LED (as shown in Table S4). Fig. 6b and S14a demonstrate that increasing power resulted in higher  $I_U$  (%), and consequently higher  $k$  values. The highest degradation rate

( $k = 9.7 \times 10^{-4} s^{-1}$ ) was achieved with 37%  $I_U$  using the low powered (3.48 V) LED power (as shown in Fig. S14a). These results suggest that higher light intensity enhances the photoreaction response, as it accelerates the redox reaction of electrons and holes by promoting the separation of  $e^-h^+$  pairs.

To maintain a constant light delivery (i.e., 3.48 V to the LED to achieve 37%  $I_U$ ), the current density was intentionally varied from 0.0 to  $0.6\ mA\ cm^{-2}$  (i.e., applied potential from 0.4 to 1.0 V vs. Ag/AgCl). Fig. 6c and S15b show minimal benzoate ion removal ( $k = 2.7 \times 10^{-4} s^{-1}$ ) at  $0.0\ mA\ cm^{-2}$ , whereas applying currents up to  $0.6\ mA\ cm^{-2}$  improved benzoate ion removal achieving higher  $k$  value (maximum  $k = 9 \times 10^{-4} s^{-1}$ ) (Figs. S14b and S15b). The ability to degrade a low molecular weight solute (i.e., benzoate ion) highlights the porous nature of the NM-Nafion-PVDF layer. The porosity of this layer is also crucial for the electrolyte, enabling photo-current "within" the optoelectrode [25]. Salt ions diffuse within the porous layer, facilitating electrocatalysis within the modified POF and accelerating  $e^-$  migration, thus reducing recombination rates for enhancing the generation of ROS within the photocatalyst.

Fig. 6d, S14c, and S15c demonstrate that there was negligible benzoate ion removal ( $k = 1.5 \times 10^{-5} s^{-1}$ ) in a control experiment with neither light nor electric current. Parallel experiments were conducted using a POT-ITO/ABI in current-only (no light), light-only (photocatalysis), or PEC mode (light and current). In the PEC mode, the degradation performance was significantly improved compared to photocatalysis or applied current alone. With a current density of  $0.66\ mA\ cm^{-2}$  and a light intensity of 37%  $I_U$ , the PEC system removed 68% of the benzoate after 60 min ( $k = 2.8 \times 10^{-4} s^{-1}$ ). This is an improvement compared to the photocatalysis system and the applied current system alone. However, Fig. 6d shows the best performance was



achieved in the PEC mode ( $k = 9 \times 10^{-4} \text{ s}^{-1}$ ) following the same mechanism with photocatalysis, indicating the synergistic effect of both photocatalysis and applied current to enhance the generated carriers and e<sup>-</sup> migration efficiently, minimizing recombination impacts while degrading the pollutant.

Furthermore, to further assess the degradation capabilities of our POF-ITO/ABI optoelectrode, we replaced the target pollutant with organic dyes (i.e., methyl blue (MB) and methyl orange (MO)). These dyes were chosen to investigate their degradability and the resulting color changes after photoelectrocatalysis. As shown in Figs. S16, the rate constant of MB ( $k = 2.2 \times 10^{-3} \text{ s}^{-1}$ ) and MO ( $k = 1.2 \times 10^{-3} \text{ s}^{-1}$ ) under photoelectrocatalysis was  $> 2\times$  higher than the photocatalytic degradation. Importantly, both organic dyes exhibited complete removal, nearly  $\sim 100\%$ , and resulted in colorless solutions after 60 min of PEC experiments. This compelling result unequivocally showcases the remarkable versatility of our optoelectrode fiber in degradation applications while also highlighting its superior performance in integrating photocatalysis and electrochemistry.

The reusability and durability of the optoelectrode are essential to demonstrate its practical application. To this end, benzoate ion oxidation using the POF-ITO/ABI optoelectrode as a PEC system with an applied potential of 1.2 V vs. Ag/AgCl (i.e., irradiated by 2.18 W LED) was performed multiple times, repeating the experiments with the same optical fiber and replacing the test solution between runs. Figs. S14d and S15d showed that there was approximately 92% benzoate ion degradation after 60 min across all five individual experiments and the  $k$  values for benzoate ion were similar ( $p = 0.44$ ). This indicates that the PEC-POF system is stable and does not decompose over time, making it a promising material for practical applications.

#### 4. Conclusions

The optoelectrode with a Nafion-PVDF polymeric layer containing  $\text{TAB}_3\text{Bi}_2\text{Br}_7\text{I}_2$  perovskite and ITO NMs was successfully fabricated. The POF-ITO/ABI exhibited a remarkable improvement in  $I_U$ , increasing from near zero for a bare PMMA/PVDF POF to 37% for NMs-coated POF optoelectrodes. These results suggest that the POF architecture exhibits exceptional light harvesting capabilities, enhancing its efficiency by adding NMs. Specifically, the deposition of a thin ITO layer on the POF surface enhanced its conductivity, allowing the original insulated optical fiber to function as a novel optoelectrode architecture, achieving very high current density ( $0.66 \text{ mA cm}^{-2}$ ) that are ideal for PEC applications, offering design flexibility over traditional ITO glass plates.

Based on the improved optical/electronic performance of POF-ITO/ABI, we achieved excellent removal efficiency of the target pollutant (benzoate ion) from water through the generation of reactive species (i.e.,  $\text{h}^+$ ,  $\text{O}_2^{\cdot-}$ ,  $\text{OH}^{\cdot}$  radicals), outperforming photocatalysis and electrocatalysis by 1.4x and 6.1x, respectively. Furthermore, increasing the surface area of PEC-POF fibers within the reactor volume could further enhance the degradation rate. This can be achieved by using a tubular reactor with high packing density of thin-diameter ( $< 1.5 \text{ mm}$ ) optoelectrodes, which provides a higher catalytic surface area ( $\text{m}^2$ ) of PEC-POF fiber per unit reactor volume ( $\text{m}^3$ ). For example, a tubular reactor with a diameter of 3 cm and a length of 30 cm can accommodate a bundle of 400 POFs, each with a diameter of 1.5 mm and a length of 30 cm. The packing density of this bundle fiber reaction is approaching  $2670 \text{ m}^2 \text{ m}^{-3}$ , which is  $> 6000\%$  higher than the rectangular glass electrode ( $3 \text{ cm} \times 30 \text{ cm}$ ) with the same size as the reactor. This is because light can be directly launched into the lumen of the POF from one end of the reactor, rather than having to pass through glass windows and water, as is the case in most current reactor systems.

The significance of this work is the development of a new functional optical electrode platform that extends the utilization region of PEC and addresses the challenges faced by traditional photoelectrocatalytic devices. The modified POF optoelectrode architecture allows the integration of different light-responsive photocatalysts, enabling natural light

PECs and improving conversion efficiency across the solar spectrum. This opens up new possibilities for more efficient and sustainable PEC systems for water purification or energy production.

#### CRediT authorship contribution statement

**Tzu-Heng Wang:** Conceptualization, Methodology, Validation, Investigation, Formal analysis, Data curation, Visualization, Writing – original draft, Writing – review & editing. **Zhe Zhao:** Conceptualization, Methodology, Validation, Investigation, Formal analysis, Data curation, Visualization, Writing – original draft. **Sergi Garcia-Segura:** Conceptualization, Methodology, Visualization, Resources, Supervision, Writing – original draft, Writing – review & editing. **Li Ling:** Conceptualization, Validation, Writing – original draft. **Ruey-an Doong:** Conceptualization, Methodology, Supervision, Funding acquisition, Project administration, Writing – original draft. **Paul Westerhoff:** Conceptualization, Methodology, Data curation, Visualization, Resources, Supervision, Funding acquisition, Project administration, Writing – original draft, Writing – review & editing. T.H.W. and Z.Z. conceived and designed the analysis, collected the data, contributed data or analysis tools, performed the analysis, and wrote the paper. S.G. S. L.L. R.A.D. and P.W. performed the analysis and wrote the paper.

#### Declaration of Competing Interest

The authors declare that they have no known competing financial interests or personal relationships that could have appeared to influence the work reported in this paper.

#### Data Availability

Data will be made available on request.

#### Acknowledgements

This work was partially funded by Ministry of Science and Technology (MOST, No. 109–2926-I-007–505), Taiwan, the National Science Foundation Nanosystems Engineering Research Center for Nanotechnology-Enabled Water Treatment (EEC-1449500) and NASA (80NSSC19C0564), and the Talent Startup Fund of Beijing Normal University (310432104). We would like to acknowledge the Eyring Materials Center at Arizona State University supported in part by the National Science Foundation (ECCS-1542160).

#### Appendix A. Supporting information

Supplementary data associated with this article can be found in the online version at doi:10.1016/j.apcatb.2023.123397.

#### References

- [1] Z. Wang, S. Xu, J. Cai, J. Ma, G. Zhao, Perspective on photoelectrocatalytic removal of refractory organic pollutants in water systems, *ACS EST Eng.* 2 (6) (2022) 1001–1014.
- [2] J.R. Hemmerling, A. Mathur, S. Linic, Design principles for efficient and stable water splitting photoelectrocatalysts, *Acc. Chem. Res.* 54 (8) (2021) 1992–2002.
- [3] H. Bian, D. Li, J. Yan, S. Liu, Perovskite – a wonder catalyst for solar hydrogen production, *J. Energy Chem.* 57 (2021) 325–340.
- [4] S. Garcia-Segura, E. Brillas, Applied photoelectrocatalysis on the degradation of organic pollutants in wastewater, *J. Photochem. Photobiol. C. Photochem.* 31 (2017) 1–35.
- [5] X.C. Mexg, Z.H. Zhang, X.G. Li, Synergetic photoelectrocatalytic reactors for environmental remediation: a review, *J. Photochem. Photobiol. C. Photochem.* 24 (2015) 83–101.
- [6] H. Wu, H.L. Tan, C.Y. Toe, J. Scott, L.Z. Wang, R. Amal, Y.H. Ng, Photocatalytic and photoelectrochemical systems: similarities and differences, *Adv. Mater.* 32 (18) (2020) 1904717.
- [7] Y. Wu, L. Zhong, J. Yuan, W. Xiang, X. Xin, H. Liu, Photocatalytic optical fibers for degradation of organic pollutants in wastewater: a review, *Environ. Chem. Lett.* 19 (2020) 1335–1346.

- [8] Y. Song, L. Ling, P. Westerhoff, C. Shang, Evanescent waves modulate energy efficiency of photocatalysis within TiO<sub>2</sub> coated optical fibers illuminated using LEDs, *Nat. Commun.* 12 (2021), 4101.
- [9] Z. Zhao, M. Lanazrini-Lopes, E. Westerhoff, X.X. Long, H. Rho, Y.Q. Bi, L. Ling, P. Westerhoff, Evanescent wave interaction with nanoparticles on optical fiber modulate side emission of germicidal ultraviolet light, *Environ. Sci. Nano* 8 (2021) 2441–2452.
- [10] L. Ling, H. Tugaoen, J. Brame, S. Sinha, C. Li, J. Schoepf, Coupling light emitting diodes with photocatalyst-coated optical fibers improves quantum yield of pollutant oxidation, *Environ. Sci. Technol.* 51 (2017) 13319–13326.
- [11] H. Wang, Y. Xiong, C. Wu, H. Zhu, Y. Chen, F. Xu, Optical fiber tip integrated photoelectrochemical sensors, *Opt. Express* 30 (2020) 6818–6825.
- [12] N. Cennamo, M. Pesavento, L. Zeni, A review on simple and highly sensitive polymer optical fiber probes for bio-chemical sensing, *Sens. Actuators B: Chem.* 331 (2021), 129393.
- [13] K.S. Schanze, P.V. Kamat, P. Yang, J. Bisquert, Progress in perovskite photocatalysis, *ACS Energy Lett.* 5 (2020) 2602–2604.
- [14] W. Wang, M.G. Xu, X.M. Xu, W. Zhou, Z.P. Shano, Perovskite oxide-based electrodes for high-performance photoelectrochemical water splitting, *Angew. Chem. Int. Ed.* 59 (1) (2020) 136–152.
- [15] J.Z.Y. Tan, N.M. Nursam, F. Xia, M.A. Sani, W. Li, X.D. Wang, R.A. Caruso, High-performance coral reef-like carbon nitrides: synthesis and application in photocatalysis and heavy metal ion adsorption, *ACS Appl. Mater. Interfaces* 9 (2017) 4540–4547.
- [16] T.B. Nguyen, P.N.T. Ho, C.W. Chen, C.P. Huang, R.A. Doong, C.D. Dong, A Z-scheme NiCo<sub>2</sub>O<sub>4</sub>/S codoped 1D g-C<sub>3</sub>N<sub>4</sub> heterojunction for solar-light-sensitive photocatalytic degradation of antibiotics in aqueous solutions exemplified by tetracycline, *Environ. Sci. Nano* 9 (2021) 229–242.
- [17] F. Ghamari, D. Raoufi, J. Arjomandi, Influence of thickness on crystallographic, stereometric, optoelectronic, and electrochemical characteristics of electron-beam deposited indium tin oxide thin films, *Mater. Chem. Phys.* 260 (2021), 124051.
- [18] X. Zheng, X. Qiao, F. Luo, B. Wan, C. Zhang, Low-cost high-performance NO<sub>2</sub> sensor based on nanoporous indium tin oxide (ITO) film, *Sens. Actuators B: Chem.* 346 (2021), 130440.
- [19] J. Zhang, A. Li, B. Li, M. Yang, X. Hao, L. Wu, Top-seed solution-based growth of perovskite Cs<sub>3</sub>Bi<sub>2</sub>I<sub>9</sub> single crystal for high performance X-ray detection, *ACS Photonics* 9 (2020) 641–651.
- [20] C.Y. Toe, J. Pan, J. Scott, R. Amal, Identifying key design criteria for large-scale photocatalytic hydrogen generation from engineering and economic perspectives, *ACS EST Eng.* 2 (6) (2022) 1130–1143.
- [21] N. Singh, B.R. Goldsmith, Role of electrocatalysis in the remediation of water pollutants, *ACS Catal.* 10 (2020) 3365–3371.
- [22] C.G. Lee, H. Javed, D.N. Zhang, J.H. Kim, P. Westerhoff, Q.L. Li, P.J.J. Alvarez, Porous electrospun fibers embedding TiO<sub>2</sub> for adsorption and photocatalytic degradation for water pollutants, *Environ. Sci. Technol.* 52 (2018) 4285–4293.
- [23] A.H.C. Khavar, G. Moussavi, A.R. Mahjoub, M. Statari, P. Abdolmaleki, Synthesis and visible-light photocatalytic activity of In, S-TiO<sub>2</sub>@rGO nanocomposite for degradation and detoxification of pesticide atrazine in water, *Chem. Eng. J.* 345 (2018) 300–311.
- [24] S. Lotfi, K. Fischer, A. Schulze, A.I. Schafer, Photocatalytic degradation of steroid hormone micropollutants by TiO<sub>2</sub>-coated polyethersulfone membranes in a continuous flow-through process, *Nat. Nanotechnol.* 17 (2022) 417–423.
- [25] F. Ghamari, D. Raoufi, J. Arjomandi, Influence of thickness on crystallographic, stereometric, optoelectronic, and electrochemical characteristics of electron-beam deposited indium tin oxide thin films, *Mater. Chem. Phys.* 260 (2021), 124051.